
This manuscript is a **preprint** and has been submitted to be considered for publication in **Earth and Planetary Science Letters**. This version of the manuscript has not undergone peer review. Content in subsequent versions of this manuscript may differ from this version of the work.

Please contact James Wood (james.wood18@imperial.ac.uk) or any of the study co-authors directly for questions relating to the manuscript.

22nd December 2025

Offshore basin evolution and normal fault migration in the western North Gulf of Evia rift

James Wood¹, Rebecca E. Bell¹, Alexander C. Whittaker¹, Saoirse M. Coveney¹, Frank Chanier², Fabien Caroir³, Haralambos D. Kranis⁴, Athanassios Ganas⁵

¹ Department of Earth Science & Engineering, Imperial College London, London, UK

² Laboratoire d'Océanologie et de Géosciences, Univ. Lille, CNRS, Univ. Littoral Côte d'Opale, Lille, France

³ Institut des Sciences de la Terre de Paris, Sorbonne Université, CNRS-INSU, Paris, France

⁴ Department of Dynamic, Tectonic & Applied Geology, National and Kapodistrian University of Athens, Athens, Greece

⁵ Institute of Geodynamics, National Observatory of Athens, Athens, Greece

Corresponding author: James Wood (james.wood18@imperial.ac.uk)

13 Abstract

14 Active extension in the North Gulf of Evia, Central Greece is contemporaneous with the
15 well-studied Gulf of Corinth but displays a contrasting style of complex rifting with marked
16 rotational and strike-slip influence from the North Anatolian Fault. We develop a late-
17 Quaternary, syn-kinematic sedimentary age model for the Western Basin of the North Gulf of
18 Evia using 2D seismic reflection data. Seismic stratigraphic principles are used to identify
19 three key horizons based on reflection termination relationships with ages of ~12 ka, ~130 ka
20 and ~325 ka assigned using a sequence stratigraphic model on deltaic clinoform packages.
21 The age model is applied across the basin alongside a network of offshore faults to determine
22 the major structural components, depocenters and evolutionary history of the rift system. We
23 resolve the major controlling faults in the basin to be the Kalypso Fault (~4 mm/yr slip) on
24 the southern margin and the Central Graben (~1-2 mm/yr slip) along the axis of the gulf. We
25 show that the Kalypso Fault is linked to the onshore Coastal Fault System, one of the most
26 active normal fault zones of the rift. The timing of initiation of the Kalypso Fault is
27 constrained to ~325 ka based on thickening relationships of syn-kinematic sediments
28 following a strain localisation (i.e. migration) event with evolving strike from the onshore,
29 Arkitsa Fault. The age model and fault network outlined here aim to further unlock detailed
30 work in the gulf to answer key questions on normal fault behaviour, rift evolution, and
31 associated geohazards in complex settings.

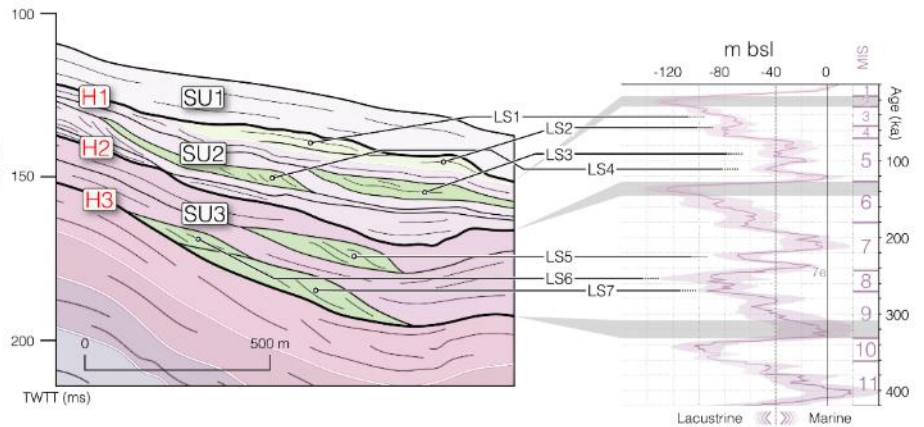
32

33 Graphical Abstract

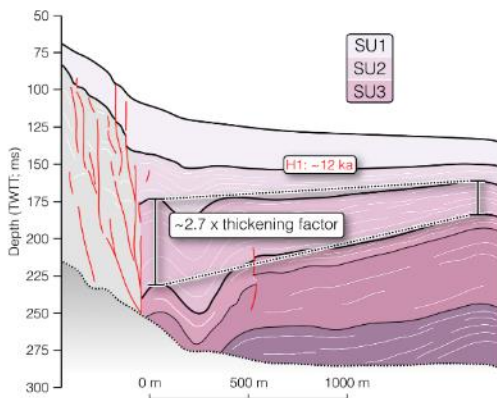
The North Gulf of Evia rift:
Tectonic overview map



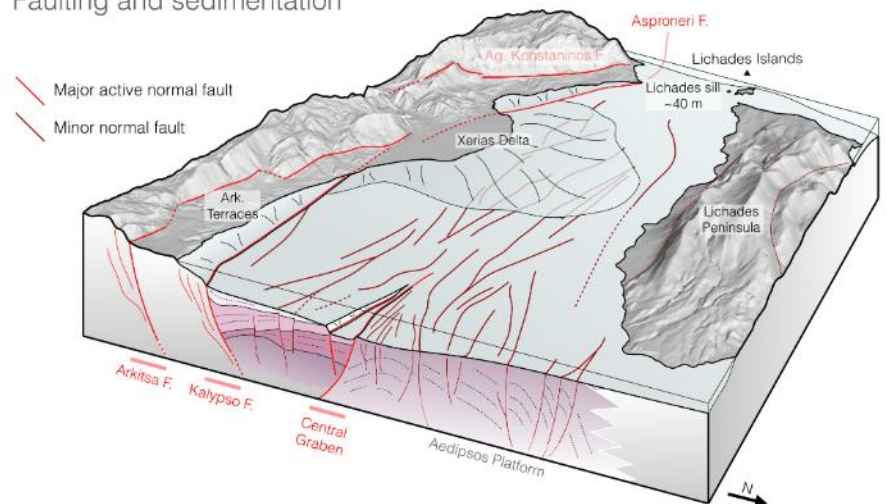
Methods - Age model:
Seismic and sequence stratigraphy (0 - 325 ka)



The Kalypso Fault:
Major offshore syn-kinematic
normal fault zone



Western Basin overview:
Faulting and sedimentation



34 1. Introduction

Understanding the timing of fault initiation and strain localisation in rifts is of key importance for constraining models of continental extension, syn-tectonic basin evolution, and seismic hazard. However, as young continental rifts are some of the most dynamic tectonic systems on Earth (Brune et al., 2023), any detailed reconstruction of the timing of fault initiation, linkage and migration demands a high-resolution age model of syn-kinematic stratigraphy (Gawthorpe and Leeder, 2000).

Syn-rift sedimentation in evolving rift basins, typically imaged at depth with seismic reflection data, provides an integrated, but often complex, record of both tectonic and environmental forcing (Gawthorpe and Leeder, 2000). Isolating tectonic signals through the reconstruction of prevailing environmental conditions (e.g., base level) can provide powerful quantitative insight into slip rates and evolution of normal fault systems (e.g., Bell et al., 2009, 2008; Feng et al., 2016; Gawthorpe et al., 2018; Nixon et al., 2024, 2016).

However, age models of active rift sedimentation at sufficient detail to allow fault slip rates and timings of initiation, linkage and migration to be resolved over high-resolution timescales (10^3 - 10^4 years) are sparse. The Gulf of Corinth, Greece represents one of the only marine continental rift systems with a high-resolution age model thanks to extensive high-resolution seismic reflection datasets (see Nixon et al., 2016) and deep offshore drilling (McNeill et al., 2019; Nixon et al., 2024). The age models developed for the Gulf of Corinth generated a framework for this rift to become one of the foremost natural laboratories for the detailed study of normal faulting processes (e.g., Bell et al., 2017; de Gelder et al., 2019; Fernández-Blanco et al., 2019; Mildon et al., 2024) and basin sedimentation (e.g., Gawthorpe et al., 2017; McNeill et al., 2019; Watkins et al., 2018).

The North Gulf of Evia, located ~100 km north of the Gulf of Corinth, represents a key extensional system in Greece that provides an excellent example of a contrasting style of rifting to Corinth. Here, the extensional system is complicated by marked rotational and strike-slip influence from the westward-propagating North Anatolian Fault (Caroir et al., 2024; Ganas et al., 2016; Sboras et al., 2025) while strike-slip associations in the Gulf of Corinth are limited (Bell et al., 2009). Temporal and spatial reconstructions of normal fault dynamics from natural examples in complex and rotational rift settings such as this are extremely limited at present. Consequently, high resolution age models of basin stratigraphy

are required to unlock detailed study into the geodynamics and mechanics of continental rifting in such settings.

In this study we utilise a high-density, high-resolution 2D seismic reflection dataset to develop a consistent seismic and sequence stratigraphic age model for late-Quaternary syn-tectonic sedimentation (0 – ~325 ka) of the Western Basin of the North Gulf of Evia rift system (Figure 1b). From this age model, we reconstruct a detailed, late-Quaternary history of fault slip and basin development to explore normal fault migration in the rift, drawing comparison to the Gulf of Corinth rift.

2. Geological Background

2.1 Tectonic setting

The North Gulf of Evia is one of a series of young, ~E-W striking rift systems spanning the continental block of mainland Greece (Figure 1a; Goldsworthy et al., 2002; Papanikolaou, 2021; Roberts and Ganas, 2000; Roberts and Jackson, 1991). Extension is thought to be controlled by the rollback of a shallowly subducting African Plate (Jolivet et al., 2013) with regional influence from the westward-propagating North Anatolian Fault (Caroir et al., 2024; Goldsworthy et al., 2002; Hatzfeld et al., 1999; Sboras et al., 2025). This influence is responsible for 5-8°/Myr rotation of the continental block between the gulfs of Evia and Corinth (Bradley et al., 2013; Chousianitis et al., 2024) and the extensive strike-slip associations in the North Gulf of Evia (Figure 1b; Caroir et al., 2024; Ganas et al., 2016; Kranis et al., 2001; Palyvos et al., 2006).

Although modern geodetic opening rates of 2.9-3.7 mm/yr (Sboras et al., 2025) are ~4x slower than in the neighbouring Corinth Rift (Briole et al., 2021; Chousianitis et al., 2024), large, damaging earthquakes are known to have occurred around the North Gulf of Evia

including the 1894 Atalanti events (Mw 6.4-6.9; Ganas et al., 1998; Pantosti et al., 2004) and the unattributed tsunami-generating earthquake of 426 BCE (Freitag and Reicherter, 2019).

The modern tectonic geometry of the North Gulf of Evia is divided into the Western, Central and Eastern Basins based on bathymetric and subsurface character (Sakellariou et al., 2007; Fig. 1b). Here we consider the Western Basin, a sub-basin at the margin of the gulf between the Coastal Fault System and the Lichades Peninsula (Figure 1c) with the highest extensional strain accommodation in the gulf (~ 3.7 mm/yr; Sboras et al., 2025). The Coastal Faults span from Arkitsa to beyond Kammena (*or Kamena*) Vourla (~ 30 km) as a segmented but linked onshore active normal fault array with a late-Quaternary footwall-component uplift rate of 0.2-0.6 mm/yr (Whittaker and Walker, 2015). The fault system is typically considered the most active structure of the modern rift (Goldsworthy et al., 2002; Roberts and Jackson, 1991). The segments of the Coastal Faults vary in orientation and dip but ubiquitously display north-oriented slip vectors (Figure 1c; Kranis 2007).

Despite evidence for Holocene slip on the Coastal Faults (Kranis, 2007), the geomorphology of the hanging wall land strip shows evidence for rapid uplift (c.f. Wood et al., 2025). This includes the uplifted marine terraces at Arkitsa (Figure 1c) and Holocene coastal notches at Kynos (Supplemental Figure S1) which may indicate the dominant normal faults have migrated offshore (Papanastassiou et al., 2014; Pirazzoli et al., 1999).

2.2 Pleistocene palaeoenvironment

Sedimentation in basins is a record of prevailing relative sea, lake or river level (Vail et al., 1977). Isolating tectonic signals from the sedimentary packages imaged in seismic reflection data demands a comprehensive reconstruction of environmental conditions (e.g., base level, sill level and sedimentary environment).

The North Gulf of Evia is a semi-enclosed basin with distinct marine, lacustrine and brackish intervals over the late-Quaternary controlled by sills in the Oreoi and Lichades Straits at 40-45 m bsl (below mean sea level; Figure 1c). Intervals where eustatic sea level is below sill level are interpreted as lacustrine or brackish in the Gulf and eustatic highstands above ~40 m bsl are considered marine. It is probable that most of the Pleistocene lakes of the North Gulf of Evia were restricted to the deepest part of the basin where many submerged terraces have been mapped in vintage seismic datasets (Van Andel and Perissoratis, 2006).

The sill level at Lichades (Figure 1c) has likely varied over time. InSAR-derived ground motion data indicates ~1 mm/yr of uplift over 2019-2023 on the island of Lichades and the coastal land strip at Kammena Vourla (Wood et al., 2025). The shallowing of the sill has been independently inferred through analysis of Pleistocene microfossil assemblages (Drinia et al., 2014).

The main fluvial drainage of the rift system, the Sperchios River (Figure 1b) reflects a closed sedimentary system throughout the Holocene with all transported sediment deposited in its delta at the Maliakos Gulf (Pechlivanidou et al., 2018). During lowstand conditions, the river likely drained through the Oreoi Channel (Figure 1b), although it is possible that drainage fluctuated to the endorheic North Gulf of Evia Pleistocene lakes where deltaic packages are resolved in seismic reflection data (Caroir et al., 2024; Van Andel and Perissoratis, 2006).

The Western Basin therefore likely alternated between a sedimentary sink and fluvial transfer zone depending on prevailing base level and rate of accommodation generation, representing a key contrast to the Gulf of Corinth where basin geometry is largely stable across lacustrine and marine intervals (Gawthorpe et al., 2018).

133 3. Data and Methods

134 3.1 Seismic data and stratigraphic age model

135 Here, a high density, high resolution seismic reflection dataset across the Western Basin is
136 used to explore the sedimentary and tectonic development of the sub-basin in detail (WATER
137 I and II; Chanier and Gaullier, 2017; Chanier and Watremez, 2021; Figure 1c, Supplementary
138 Figure S5). The WATER surveys acquired ~1800 km of single channel sparker (50-300 J)
139 seismic profiles across the North Gulf of Evia, Oreoi Channel and Skopelos Basin. The
140 subset of 41 profiles used in this study are ca. 350 ms at maximum interpretable depth (~260
141 – 320 m) and data is typically interpreted to the first seabed multiple which obscures the
142 signal below. Seismic velocities are modelled as 1500 m/s for seawater and 1800 m/s for
143 depth conversions consistent with Caroir et al. (2024).

144 The WATER dataset has been studied previously to determine the regional structural anatomy
145 of the North Gulf of Evia and show the influence of strike-slip deformation at the western
146 termination of the North Anatolian Fault (Caroir et al., 2024). However, no pre-Holocene age
147 correlations have been made for the sedimentary stratigraphy in the offshore North Gulf of
148 Evia to date.

149 In this study, key seismic horizons (H1-H3) are identified in the dataset based on seismic
150 terminations including onlap relationships and erosive truncation (Catuneanu, 2002; Vail et
151 al., 1977). Between these horizons, seismic units (SU1-3) are defined and each unit is
152 characterised based on seismic attributes and geological significance, consistent with seismic
153 facies principles (Vail et al., 1977; Xu and Haq, 2022). Three-dimensional surfaces are
154 produced from the key seismic horizons to analyse spatial variability of sediment package

155 thickness across the gulf (Supplementary Figure S3) with isopachs for each SU calculated as
156 the difference between two surfaces.

157 Age estimates for the seismic horizons and units are derived from sequence stratigraphic
158 principles as unconformity-bounded sediment sequences at the margins of marine and
159 lacustrine systems preserve a record of relative base level change (Catuneanu, 2002; Vail et
160 al., 1977). In clastic systems at basin margins, deltas build up (i.e., aggrade) to prevailing
161 base level before growing outwards (i.e. prograde). When preserved in the geologic record,
162 these packages can be used to infer the sequential timing of local highstand and lowstand
163 periods (Catuneanu, 2002). For late-Quaternary sedimentation, well constrained eustatic sea
164 level curves (e.g., Spratt and Lisiecki, 2016) can be correlated to sequences of clinoforms to
165 generate age models for basin sedimentation (e.g., Bell et al., 2008; Lykousis et al., 2007a).

166 In the south of the Western Basin, a well-developed sequence of submerged clinoform
167 packages is found on seismic lines 107 and 049. These packages are used to establish age
168 estimates for seismic horizons through correlation to the sea level curve of Spratt and Lisiecki
169 (2016; Figure 2 and 3). Distinct clinoform package rollover points (i.e. topset to foreset
170 transition) are identified in seismic profiles and act as markers of past marine or lacustrine
171 relative base level in the gulf (Catuneanu, 2002). To establish if a clinoform package best
172 correlates to a highstand or lowstand interval, package geometry, apparent base level and
173 stratigraphic sequencing are considered (Catuneanu, 2002; Figure 2a and 2b). Packages are
174 defined as lowstands if they sit stratigraphically above a package with a higher indicated base
175 level or show an exaggerated sigmoidal geometry consistent with decreasing/low
176 accommodation (Figure 2a). Highstand sequences are defined if they build up to higher base
177 level than the underlying stratigraphic package (Figure 2b). Ages are provided with reference
178 to Marine Isotope Stages (MIS) and numeric values are assigned from the sea level stack of
179 Spratt and Lisiecki (2016).

Sill level is marked on base level diagrams at 40 m bsl and at a level consistent with an uplifting sill at 0.1 mm/yr (i.e. 10 year period of 1 mm/yr uplift every 100 years; Wood et al., 2025). Base levels below sill level are considered lacustrine and above are considered marine.

3.2 Identification and classification of normal faults

Offshore faults are identified in seismic reflection profiles and mapped across lines to generate three-dimensional geometries. Structures are classified on the most recent key seismic horizon (H1-H3) they offset, providing an estimate for most recent activity. Fault throw is measured as the vertical offset of the key dated seismic horizons defined in the age model across each structure and represents the maximum observable throw on each fault over the given time interval. Throw rates are converted to slip rates with an assumed fault dip of 60-70°, consistent with measured fault planes on the Arkitsa Fault (Kranis, 2007). The full fault database is summarised in more detail in the supplementary material (Figure S4; Table S1 and S2).

Geological field work was conducted in April and October 2025 and included corroborating previous works, refining onshore fault maps (Figure 1) and documenting evidence for onshore uplift and young normal faulting within syn-rift stratigraphy (Supplementary Figure S1).

4. Results

4.1 Seismic stratigraphy

Three major stratigraphic horizons are identified based on the observation of erosional truncation, onlap terminations and significant changes in seismic character (H1, H2 and H3;).

201 These surfaces can be seen on the seismic profiles of Figure 2c and 3 and their character is
202 summarised in Figure 4.

203 Both H1 and H2 are highly erosive with overlying sediments commonly onlapping these
204 surfaces (Figure 2 and 3). These horizons each represent a depositional hiatus in the gulf,
205 representing extended periods of subaerial erosion when the North Gulf of Evia lake was
206 restricted to the deep Central basin (Van Andel and Perissoratis, 2006).

207 A significant change in seismic facies occurs across surface H3 (Figure 4). Younger,
208 overlying sediments are dominated by high amplitude reflectors and abundant clinoforms
209 while below H3, reflections are dominantly low amplitude punctuated by thin, high amplitude
210 packages (Figure 4 and 5). In places, overlying reflections onlap H3 (Figure 5b).

211 H1 to H3 bound three seismic units defined in Figure 4 (SU1-3). SU1 is found between the
212 seabed and H1. It is dominated by acoustically transparent fan deposits with a thin, high
213 amplitude drape elsewhere. SU1 is equivalent to the Upper Sequence of Caroir et al. (2024)
214 which is considered to represent Holocene sedimentation in that study. Shallow coring of this
215 seismic unit in the Central Basin has confirmed the Holocene age of these sediments (Drinia
216 et al., 2014; Sakellariou et al., 2007). The fan deposits that dominate the Western Basin are
217 derived from the Xerias River (Figure 1c; Van Andel and Perissoratis, 2006). The erosive
218 surface H1 therefore formed during the Last Glacial Maximum (MIS 2, ~12 ka).

219 SU2 is found between H1 and H2. It is highly variable in thickness, owing to erosive surfaces
220 at both the base (H2) and top (H1) of the unit and is characterised by abundant clinoforms
221 and onlapping reflectors (Figure 4 and 5). The reflections in the unit are typically high
222 amplitude which, based on seismic reflections and age correlations in the Gulf of Corinth
223 (e.g., Bell et al., 2008; Nixon et al., 2016), implies highstand conditions dominate
224 sedimentation during this time.

SU3, between H2 and H3, is similarly characterised by high amplitude reflections but tends to be more laterally continuous and lower frequency than SU2 with fewer clinoforms (Figure 4). The unit, in deeper basin settings transitions from high amplitude to low amplitude while in marginal depositional settings is nearly exclusively high amplitude with abundant internal and external onlap relationships (Figure 5). SU3 unit is interpreted to represent highstand sedimentation in a marginal sub-basin prior to subaerial exposure and the formation of H2.

4.2 Sequence stratigraphy

Sequence stratigraphy of deltaic clinoform packages in Figure 2 and 3 is used to attribute ages to the seismic stratigraphy outlined above through correlation to expected base level in the gulf. Within the sedimentary succession spanning H1 to H3 shown in Figure 2c and 2d, nine distinct packages are identified. Based on the ordering of apparent relative base levels and sequence geometries outlined in the schematic diagrams of Figure 2a and 2b, each package is classified as a relative lowstand or highstand.

Seven lowstand indicators are interpreted between 98 and 135 m bsl (LS1-LS7). These packages have cross-sectional widths of 200-600 m with heights of ~10-20 ms (~9-18 m). LS1 and LS2 sit directly below H1 and indicate similar relative base levels of 98 and 109 m respectively. As H1 very likely represents the base-Holocene surface (see section 4.1), these clinoforms must have developed during moderately high lake level or brackish deposition in MIS 3 at a base level between sill level and ~80 m bsl (Figure 2d). Lake levels in both MIS 2 and MIS 4 were restricted to the Central Basin (Figure 1b; Van Andel and Perissoratis, 2006) so deltaic clinoforms are unlikely to have developed in this part of the Western Basin during those intervals.

HS1, LS3, HS2 and LS4 follow in the stratigraphic sequence and compose the remaining strata of SU2. HS1 and HS2 are interpreted as highstands as both aggradation of >40 m and

retreat towards the basin margin of ~1.2 km are resolved for these packages (see comparison to Figure 2b). The rollover of HS1 is not imaged here so the apparent relative base level of ~70 m bsl is considered a minimum possible value. LS3 (~118 m bsl) sits stratigraphically above HS1 while LS4 (~114 m bsl) sits between HS1 and HS2 with the morphologies and stratigraphic relationships of the two lowstand patterns indicative of a forced regression (see comparison to Figure 2a). The downdip extension of the HS1 package bifurcates above and below LS3 while the up-dip extent of this unit drapes HS2. Based on this sequencing, these four packages are attributed to MIS 5 with HS2 being MIS 5e and the thin sediment drape above this of HS1 likely being an amalgamation of MIS 5c and 5a. Significant local subsidence between MIS 5e and 5c is required to allow this drape at a sea level that is expected to be ~25 m lower than the extreme highstand of MIS 5e (Figure 2d). Based on sequencing relationships to these highstands, LS3 is attributed to MIS 5b and LS4 assigned to MIS 5d (Figure 2d).

Horizon H3 is located below this and, given its character as a strongly erosive surface, best represents late-MIS6 when the Western Basin likely saw an extended period of subaerial exposure following significant base level fall. Immediately below this surface is a package of consistent deposition without a preserved associated clinoform package (Figure 2c). LS5 (~126 m bsl) is a laterally restricted clinoform package with an indicated relative base level far below the underlying unit. It is therefore considered a lowstand interval (Figure 2a). LS6 (~125m bsl) is a narrow (~200m) clinoform set that builds up above the underlying package (LS7; ~135 m bsl). However, it does not build up above horizon H3 and, given aggradation from LS7 to LS6 is only ~10 m, both are considered lowstand packages. The stratigraphic positioning of LS5 best fits a moderate lowstand during MIS 7 (MIS 7d) with overlying sediment representing subsequent periods of higher sea level (i.e., MIS 7c-a). Finally, the two

273 closely related packages of LS6 and LS7 sit below a further interval of highstand
274 sedimentation (MIS 7e) and are best correlated to MIS 8.

275 Surface H3 marks the base of the interpreted clinoform packages in Figure 2c and 2d and,
276 given its nature as a cap to a high amplitude package marking a significant change in basin
277 sedimentation, is attributed to MIS 9e (Figure 2d). Correlation below H3 is uncertain due to
278 poor imaging in the seismic reflection dataset across the basin.

279 Figure 3a shows a well-developed sequence of clinoforms on an intersecting seismic profile
280 to Figure 2c (Figure 3b). All packages marked in Figure 3a are characterized as lowstand
281 intervals based on comparison to expected geometries (Figure 2a) with two packages
282 developed on the southeastern margin and four developed on the northwestern margin of a
283 small paleo-bathymetric depression. Stratigraphic sequencing here is comparable to Figure 2c
284 and all lowstand packages from Figure 2c are represented in this adjacent line, except LS2
285 which is not locally developed. Indicated base levels in Figure 3a are within 10% of
286 counterparts in Figure 2c for each resolved lowstand package except LS1 which has an
287 indicated depth of 17 m lower. This may imply heightened tectonic subsidence has occurred
288 at the southeastern end of this profile.

289 Based on this sequence stratigraphic model across both Figure 2 and 3, age estimates of H1-3
290 and SU1-3 are derived and attributed to the seismic stratigraphic architecture of Figure 4. In
291 short, H1 represents MIS 2 (~12 ka), H2 represents late-MIS 6 (~130 ka) and H3 represents
292 MIS 9e (~325 ka).

293 Key to the utility of the age model is that it can be mapped consistently across the Western
294 Basin and wider North Gulf of Evia. Figure 5 shows interpreted seismic profiles that span the
295 axial length of the Western Basin (Figure 5a) and cross the width of the study area (Figure
296 5b) with the age model of Figure 4 applied. The erosive nature of H1 and H2 and the acoustic

transparency of SU1 are well highlighted in Figure 5a and the onlapping relationships of H1-3 are highlighted in the south of Figure 5b. The marked change in seismic expression beneath horizon H3 is evident in across both profiles with a shift from high amplitude reflections dominating above to low amplitude reflections below. Where apparent in Figure 5a, clinoforms are restricted to SU2 and SU3 with indicated paleo-flow directions to the west. A substantial (~2 km wide) clinoform package attributed to MIS 5e on line 229 also indicates flow to the west. These flow directions are opposed to expected drainage to the southeast based on modern depocenters (Figure 1b).

4.3 Normal fault network

Application of the age model to develop a full tectonic evolutionary history of the Western Basin demands a comprehensive map of offshore normal faults. Figure 6a and 6b show the mapped offshore fault network from this study. 47 offshore fault segments are mapped with lengths of 0.5 km to 12 km (see Supplementary Table S1 and S2). The structural fabric of the offshore rift is characterised by dominantly E-W striking normal faults, following the axis of the gulf (Figure 6). The density of sub-parallel normal faults across the width of the gulf increases from west to east as 3 to 4 structures span the basin near Neochori and 16 faults are mapped across the basin in the east (Figure 6a).

The base-Holocene surface (i.e. depth to H1 erosive surface) shown in Figure 6a and 6b provides a clearer indication of Pleistocene depocenters of the basin than modern bathymetry as the thick fan deposits from the Xerias River (Figure 1c) are stripped away. This surface allows primary depocenter-controlling structures to be identified.

The fault network in Figure 6a is classified on most recent evident fault slip derived from the youngest mapped horizon (H1-3) that they offset. Active faults (i.e. structures that offset H1 or the seabed) are depicted in red while faults that do not offset H1, H2 or H3 are considered

least active (grey). Figure 6b classifies each structure on the maximum resolved throw rate in this study with separate rates calculated between each age-attributed horizon (Figure 4). Only three faults exhibit throw rates of >0.75 mm/yr (F01, F08 and F10) with the highest throw rate in the basin of ~ 3.75 mm/yr during the Holocene resolved for F01. Across all normal faults, a median throw rate of 0.2 mm/yr is resolved.

The southeast of the Western Basin appears to be controlled by a single, east-northeast striking ($\sim 260^\circ$) major normal fault zone (F01), here named the Kalypso Fault (from the homonymous settlement west of Arkitsa; Figure 6a). At the eastern tip of the fault, spacing to the onshore Arkitsa Fault segment is ~ 4 km with negligible spacing between the structures in the west, particularly when the onshore continuation of the fault is considered (Figure 6a). A potentially active normal fault had previously been inferred here based on the uplifted marine terraces between the Arkitsa Fault and the modern coastline (Cundy et al., 2010; Papanastassiou et al., 2014) and the fault is mapped as WB4 in the regional structural analysis of Caroir et al. (2024). We find the onshore continuation at the western extent of the Kalypso Fault to follow a topographic escarpment (Figure 6) where fault breccia with syn-rift clasts and fault surfaces (79/025; dip/azimuth) are found (Supplementary Figure S1a).

The Central Graben, consisting of a major south dipping and north dipping normal fault (F10 and F08), is located along the axis of the gulf in the east of the study area (Figure 6). The graben opens significantly to the east with a fault spacing of 200 m at the western tip of the graben and > 2.5 km in the east (Figure 6a). The main faults of the graben appear to trend further to the east to bound the deep Central Basin, suggesting the faults are a significant modern bathymetric control in the gulf (c.f., Caroir et al., 2024). Slip is considerable on these structures with Holocene throw rates of 0.9 mm/yr on the south dipping fault and 1.7 mm/yr on the north dipping fault (Figure 6b).

The Asproneri Fault (F43) in the southwest generates a significant bathymetric escarpment and appears to be a major control on accommodation generation in this area (Figure 5b and 6a). This structure is likely responsible for uplifted terraces in the hanging wall of the onshore Agios Konstantinos Fault (Figure 1c; Supplementary Figure S1c). However, slip rates and along-strike variation for this structure are poorly resolved due to the low density of seismic profiles here (Figure 1c).

4.4 Syn-kinematic sedimentation

Integrating the sedimentary age model with the normal fault network in Figure 6 constructs a picture of how major depocenters in the Western Basin have changed over time in response to tectonic and environmental forcing. The syn-tectonic thickening of sediment packages into the hanging wall of normal faults also provides an indication of timing, and rates, of fault activity as hanging wall subsidence generates heightened accommodation space (e.g., Coveney et al., 2025; Gawthorpe and Leeder, 2000; Jackson et al., 2017). Figure 7 shows sediment thickness isopachs of the three seismic units defined in Figure 4 (SU1-3) with the thickening direction of each unit SU1-3 indicating the major structural controls on syn-rift sedimentation at the time.

Figure 7a depicts a Holocene-only (SU1) isopach. In the west, sedimentation is dominated by the ~50 m thick deposits of the Xerias Fan (Figure 1c), while in the east, Holocene sedimentation is thickest between the Kalypso Fault and a south-dipping series of faults ~3 km to the north (F02, F03, F46 – Figure 6). Elsewhere in the Western Basin, a thin drape of SU1 caps the underlying succession.

Figure 7b shows the thickness of SU2. This isopach also shows thickening towards the south and the Kalypso Fault to a maximum thickness of ~30 m. Yet, preserved sediment thickness

368 of SU2 shows high variability due to an apparently wider spatial distribution of active
369 faulting during this time and erosion from the overlying H1 unconformity.

370 Figure 7c also shows significant thickening of SU3 to the south across both the east, towards
371 the Kalypso Fault, and west, towards the Asproneri Fault. Post-depositional faulting and
372 subaerial erosion during MIS 6 (H2) and MIS2 (H1) results in similarly high variability in
373 this isopach to Figure 7b.

374 Figure 7d shows a further isopach constructed from a pre-325 ka sediment package that is
375 only correlated across the deeper southeast of the study area due to poor imaging elsewhere.
376 In contrast to the overlying units, this package shows a thickening trend towards the north,
377 showing an inverted polarity of thickening. This implies that the major control on
378 accommodation generation in the depocenter during this interval was likely the south-dipping
379 fault of the Central Graben (Figure 7d and 8).

380 These sediment thickening trends are also depicted in profile in Figure 8. Here, SU1-3 show
381 significant syn-tectonic thickening into the immediate hanging wall of the Kalypso Fault.
382 SU3, for example thickens from 20 m to 54 m over 1.5 km towards the fault zone (Figure
383 8b). Packages below SU3, such as the pre-325 ka package mapped in the isopach of Figure
384 7d, maintain constant thickness into the Kalypso fault plane and instead thicken significantly
385 towards the Central Graben in the north (Figure 8a and 8b). This provides evidence that the
386 Kalypso Fault likely initiated to become the dominant syn-sedimentary control on the
387 Western Basin immediately prior to the deposition of SU3 (~325 ka).

388 Figure 8a also directly images the fault zone of the Kalypso Fault. From the offset of the ~12
389 ka surface across the Kalypso Fault (~45 m) in this profile, a maximum Holocene throw rate
390 of ~3.75 mm/yr is resolved (Figure 8b). Considering a long-term uplift to subsidence ratio of
391 1:2-3, consistent with normal faults in the Gulf of Corinth (e.g., Armijo et al., 1996; McNeill

et al., 2005; Nixon et al., 2024), the Kalypso Fault is likely responsible for ~0.9-1.3 mm/yr footwall uplift. This is comparable to the estimated 1-1.5 mm/yr uplift rates derived for the Arkitsa marine terraces in the immediate footwall of the Kalypso Fault, based on ¹⁴C dating of shelly fauna (Papanastassiou et al., 2014).

5. Discussion

5.1 Pleistocene evolution of the Western Basin

The seismic stratigraphic age model developed in this study (Figure 4) represents the first pre-Holocene correlation proposed for the North Gulf of Evia. The age model is applicable and consistent across the Western Basin (Figure 5) and allows both for the timing of fault activity and the first estimates of Pleistocene slip rates of offshore normal faults in the North Gulf of Evia to be derived (Figure 6). This has allowed several key events in the evolution of the offshore Western Basin to be resolved as presented in the schematic evolutionary block models of Figure 9a-c.

The initiation of the Kalypso Fault at ~325 ka, depicted in Figure 9a, represents a marked change in the major depocenter geometry and structural control in the gulf with older sedimentary units showing thickening towards the axial Central Graben (Figure 7d).

Following this, base level fall and subaerial exposure of the Western Basin resulted in significant erosion (H2) and drainage reorganisation during late-MIS 6 (~130 ka; Figure 9b). A similar significant regression occurred in the gulf during MIS 2, allowing the erosive H2 seismic surface to develop (Figure 4). During these extreme lowstand intervals, the studied area represents a fluvial transfer zone for drainage towards the main sedimentary sink of the rift system in the Central Basin (Figure 9b).

The dominant westward paleo-flow direction of clinoform packages in SU1 and SU2 of Figure 5a (opposite to modern drainage) suggests that drainage reorganisation has been a common occurrence in the Western Basin throughout the late-Pleistocene.

Subsequent flooding of the basin in the Holocene has promoted the rapid progradation of the Xerias Delta, which has dominated Western Basin deposition over the Holocene (Figure 7a, 9c and 9d).

5.2 Age model comparison to the Gulf of Corinth

Comparing the age model presented in this study to similarly constructed age models for syn-rift sedimentation in the Gulf of Corinth (e.g., Bell et al., 2008; Lykousis et al., 2007b; Nixon et al., 2016) reveals a number of key similarities and differences between the rifts.

Like the offshore age models for basin sedimentation in the Gulf of Corinth (e.g., Bell et al., 2008; Nixon et al., 2016) our age model is constrained by key seismic horizons representing intervals of rapid environmental (i.e. base level) change. We define three key horizons (H1-3) while seven key horizons are defined in the Gulf of Corinth age model of Nixon et al. (2016), owing to deeper imaging of seismic reflection data there. H1 (~12 ka) and H2 (~130 ka) in our study correlate with the upper two key horizons (H1 and H2) in the Gulf of Corinth (Nixon et al., 2016). Horizon H3 from our study has a proposed age of ~325 ka and is equivalent to H4 (~340 ka) in the model of Nixon et al. (2016) with the small age discrepancy related to the position within the highstand package the horizon is placed.

The efficacy of the seismic age models of Nixon et al. (2016) and others have recently been tested following International Ocean Discovery Program (IODP) drilling in the Gulf of Corinth (McNeill et al., 2019; Nixon et al., 2024). This drilling has allowed the magneto- and bio-stratigraphic dating of Corinth seismic horizons H1 (13 ka), H2 (129 ka) and H4 (335

ka), finding the proposed ages from the existing seismic stratigraphic model to all be within 5 ka (Nixon et al., 2024).

The seismic expression of the units however highlights several differences between the Western Basin of the North Gulf of Evia and the Gulf of Corinth. Seismic units in the deep basin settings in Corinth alternate between thick low amplitude packages, correlated to lowstand lacustrine deposition, and thin high amplitude packages correlated to marine deposition during highstands (Bell et al., 2008; Nixon et al., 2024). In contrast, the late-Pleistocene seismic units in the Western Basin are near-universally characterised by high amplitude reflections (Figure 4 and 5). This reflects the exaggerated sensitivity of the North Gulf of Evia to sea level change. This sensitivity is due to a combination of the 40 m Lichades Sill to the Aegean Sea (Figure 1c; 20 m shallower than the Rion Sill to the Gulf of Corinth; McNeill et al., 2019) and the overall shallow bathymetry and palaeo-bathymetry of the Western Basin (<120 m; Figure 6). As a result, sedimentation across much of the sub-basin is restricted to interglacial highstands (e.g., MIS 5, 7 and 9) as lowstand Pleistocene glacial lakes (e.g., MIS 2 and 6) were likely confined to the deep Central Basin (c.f., Van Andel and Perissoratis, 2006). The distinct periods of subaerial exposure of the Western Basin (Figure 9b) are also not widely seen across wide areas in the basins of the Gulf of Corinth (Gawthorpe et al., 2018).

Reliable sedimentation rates are difficult to constrain in the Western Basin due to the strongly developed H1 and H2 erosive surfaces (Figure 4). It is possible to deduce, however, that sedimentation in the Western Basin is markedly slower than in the main depocenters of the Gulf of Corinth. In the well-preserved seismic packages in the south of Figure 8, where erosion appears to be minimal, sedimentation rates of 0.1-0.3 mm/yr are calculated for the thickest sections of SU3 (20-54 m over ~195 kyrs) and 0.1-0.2 mm/yr (10-20 m over ~120 kyrs) for SU2. Despite these rates likely representing maxima in the Western Basin, they are

an order of magnitude slower than sedimentation over comparable time intervals in the main depocenters of the Gulf of Corinth of 1-3 mm/yr (McNeill et al., 2019).

5.3 Normal fault migration

The overall structural anatomy of the modern Western Basin of the North Gulf of Evia reflects an asymmetric graben with dominant structural control from the onshore Coastal Faults and near-offshore Kalypso Fault (Figure 9d).

A trend of increasing recency of fault activity towards the Central Graben and Kalypso Fault is resolved (Figure 6a). Faults on the northern margin of the basin have not generated significant accommodation, nor do they show significant slip, during the deposition of SU1-3 with the major depocenters found to the south of the Central Graben (Figure 6b and 7). The Kalypso Fault represents the northernmost migration of the fault systems of the southern margin while migration from northern margin has localised on the Central Graben (Figure 6b). Holocene slip in the Central Graben is significant with ~2 mm/yr slip on the north-dipping structure and ~1 mm/yr slip on the south-dipping fault. The south-dipping fault generated significant hanging wall accommodation prior to ~325 ka (Figure 7d and 8).

Faults on the northern margin of the western basin appear to have migrated to broadly parallel structures (Figure 6a). In contrast, the main strain localisation event on the southern margin from the Arkitsa Fault to Kalypso Fault has occurred across non-parallel faults with evolving strike (Arkitsa = ~280°; Kalypso = ~260°; Figure 9d). This is interpreted to reflect the rotational influence on fault migration in the gulf. The western tip of both Arkitsa and Kalypso segments join the Agios Konstantinos Fault at the same point resulting in extremely tight fault spacing in this area (Figure 9d). It appears that this western tip has acted as a rotational axis for this strain localisation event.

The strike of the Kalypso Fault also reflects a comparable extension azimuth to the $\sim 70^\circ$ strike rupture plane resolved for the 2013 Mw = 5.4 Kallidromon earthquake sequence in the same tectonic system (Ganas et al., 2014).

Activity on the Kalypso Fault initiated at ~ 325 ka, as inferred from a reverse in thickening direction at this time towards the structure (Figure 7 and 8). The uplifted marine terrace staircase in the footwall of the structure (Figure 9; Papanastassiou et al., 2014) implies that footwall uplift of the Kalypso Fault has exceeded hanging wall subsidence of the Arkitsa Fault over the late-Pleistocene. To achieve this, the Kalypso Fault has likely undergone fault linkage to the other segments of the Coastal Fault System. This suggests the Arkitsa Fault has seen a marked reduction in slip rate since the initiation of the Kalypso, in agreement with previous work where late-Pleistocene slip on the Arkitsa Fault is reported to be as low as 0.7 mm/yr (Walker et al., 2010; Whittaker and Walker, 2015).

The Kalypso Fault, as part of the linked Coastal Fault System, presents significant seismic hazard. The fault, with a segment length of ~ 12 km (Figure 6) and a linked length of ~ 30 km to the Kammena Vourla Fault segment (Figure 1c), is capable of hosting Mw > 6 earthquakes (Wells and Coppersmith, 1994). The presence of an offshore, high slip rate structure also presents significant tsunami hazard to the North Gulf of Evia and could provide a potential source for the currently unattributed tsunami-forming event of 426 BCE (Freitag and Reicherter, 2019).

6 Conclusions

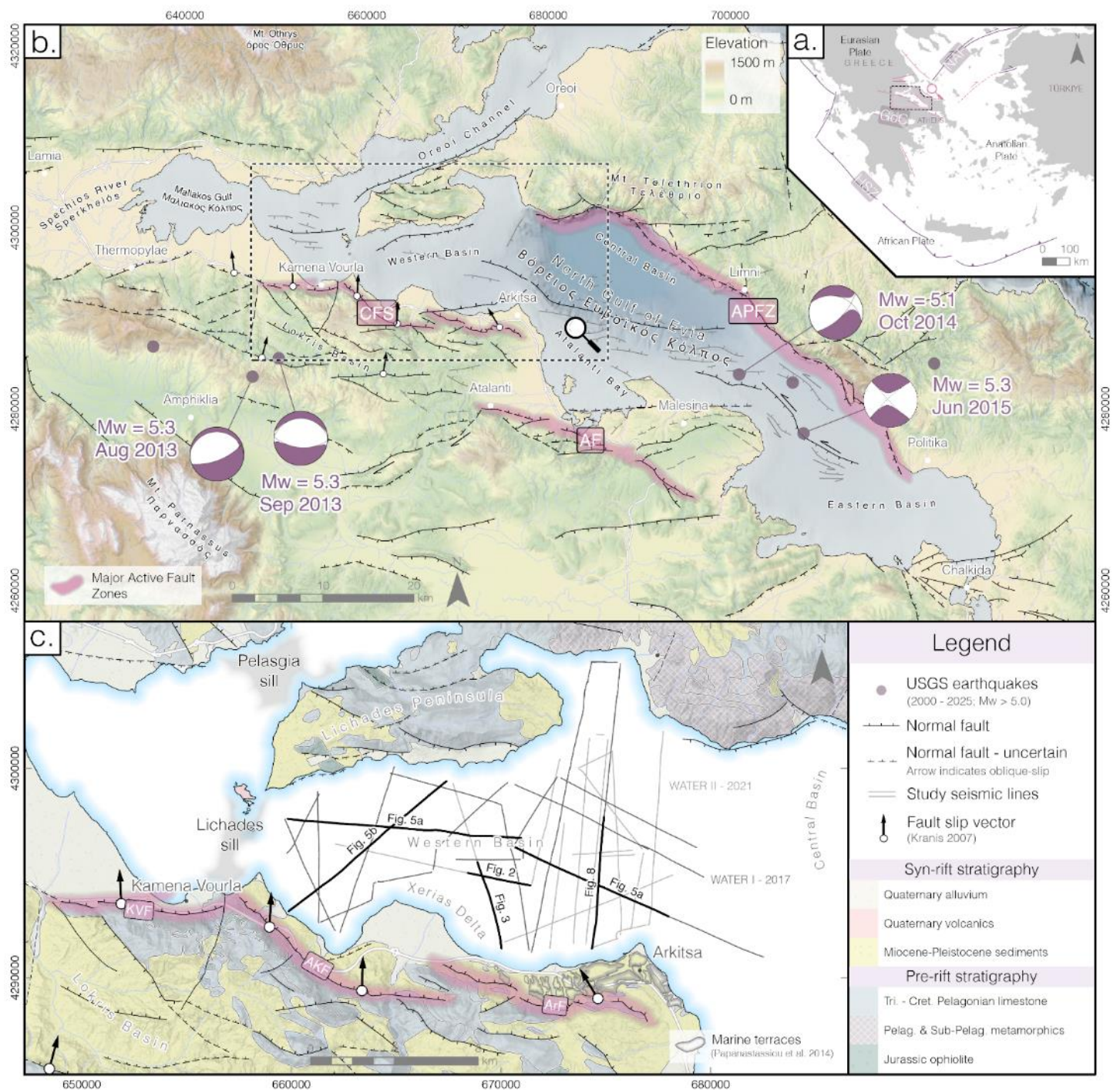
This study offers new insights into basin development, sedimentation, and normal faulting in the Western Basin of the North Gulf of Evia rift system using 2D seismic reflection data.

507 A late-Quaternary sedimentary age model for the region (0~325 ka) is proposed using
508 seismic and sequence stratigraphic principles and is found to be consistently applicable and
509 highlights spatial and temporal trends in syn-rift sedimentation, showing the main depocenter
510 now follows the southern margin of the basin.

511 A new offshore fault network is developed and combined with the age model to resolve slip
512 rates and timing of activity and fault migration in the basin. The Kalypso Fault at the
513 southeastern margin of the Western Basin is found to exert dominant structural control
514 following a strain localisation event (i.e. migration) at ~325 ka. Activity on the Kalypso Fault
515 has continued into the Holocene at a slip rate of 4.0 – 4.3 mm/yr.

516 This work aims to provide an offshore structural and stratigraphic framework for future
517 detailed studies in the North Gulf of Evia to further evaluate regional seismic hazard, syn-rift
518 sedimentary basin evolution, and geodynamic processes in complex rift settings.

519 Figures & Captions:



520

521 **Figure 1:** a) Tectonic map of the eastern Mediterranean showing major plate boundary faults.

522 NAF = North Anatolian Fault, GoC = Gulf of Corinth, HSZ = Hellenic Subduction Zone. b)

523 Regional tectonic map of the North Gulf of Evia, Central Greece. Major active normal fault

524 zones highlighted in purple. Moment tensors of recent $M_w > 5$ earthquakes from the USGS
525 database (<https://earthquake.usgs.gov/earthquakes/search/>). CFS = Coastal Fault System, AF
526 = Atalanti Fault, APFZ = Aedipsos-Politika Fault Zone. Onshore fault traces compiled from a
527 number of studies and databases (Galanakis et al., 2025; Ganas et al., 2013; Kranis, 2007)
528 and primary field study. Offshore faults from Caroir et al., (2024). c) Bedrock geology of the
529 Western Basin of the North Gulf of Evia (after IGME, 2006) and offshore seismic reflection
530 data profiles used in this study (see Supplementary Figure S5 for profile numbers). Fault slip
531 vectors after Kranis (2007) and Arkitsa terrace outlines after Papanastassiou et al. (2014).
532 KVF = Kammena Vourla Fault, AKF = Agios Konstantinos Fault, ArF = Arkitsa Fault.

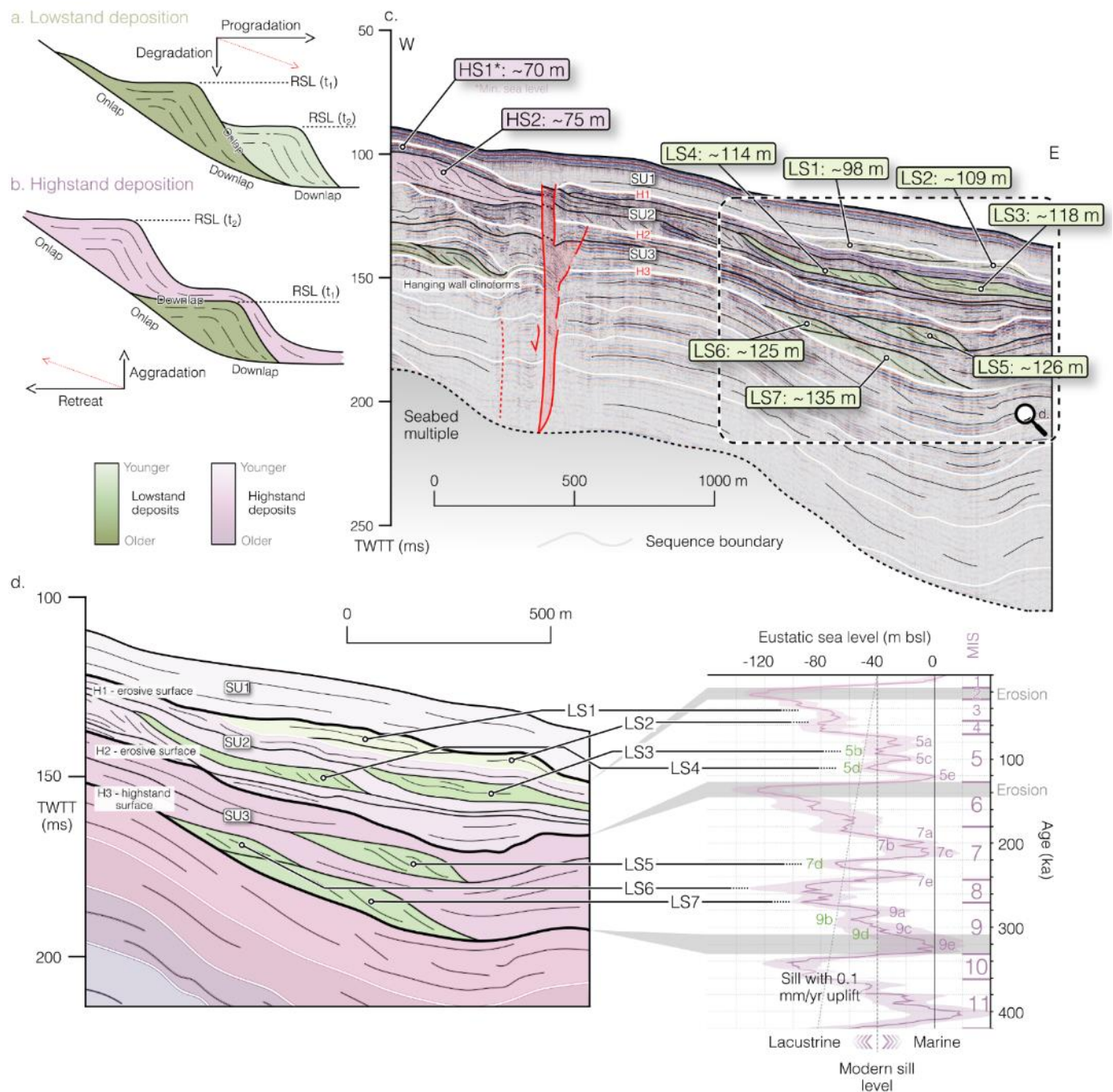


Figure 2: Schematic cartoons showing clinoform package geometries on a basin slope generated following a fall in relative sea level (RSL) from t_1 to t_2 to generate lowstand packages (a) and a rise in RSL (b) to generate highstand packages. Modified based on Catuneanu (2002). c. Seismic interpretation of Line 107 (WATER II) showing 7 identified lowstand packages and 2 marked highstand intervals. Clinoform packages shaded based on highstand or lowstand attribution. Indicated depths are the rollover point of the clinoform package (i.e. base level indicator) based on seismic velocities of 1500 m/s and 1800 m/s for

seawater and sediment respectively. Lowstand sequences are only considered for the age model in the footwall of the minor normal fault zone in the west of the seismic line. Detailed view of lowstand package interpretation with correlation to eustatic sea level curve of Spratt and Lisiecki (2016). See Supplementary Figure S6 for uninterpreted seismic section.

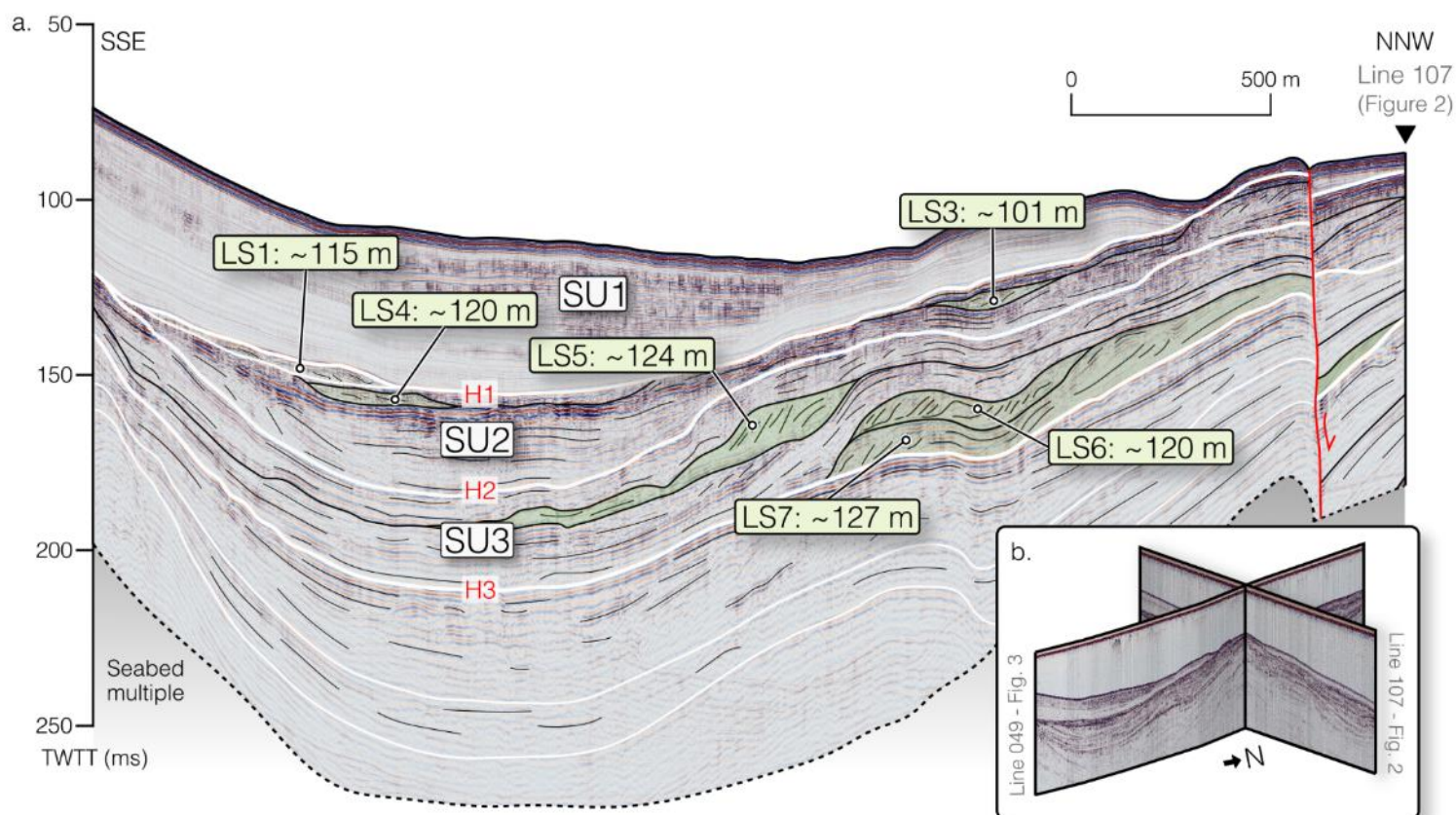


Figure 3: Seismic interpretation of Line 049 (WATER II) with the application of the sequence stratigraphic framework defined in the adjacent line (107) of Figure 2. Marked depths correspond to rollover point of clinoform package. b. 3D model showing the geometric interaction between Line 107 (Figure 2) and Line 049 shown in a. See Supplementary Figure S7 for uninterpreted seismic section.

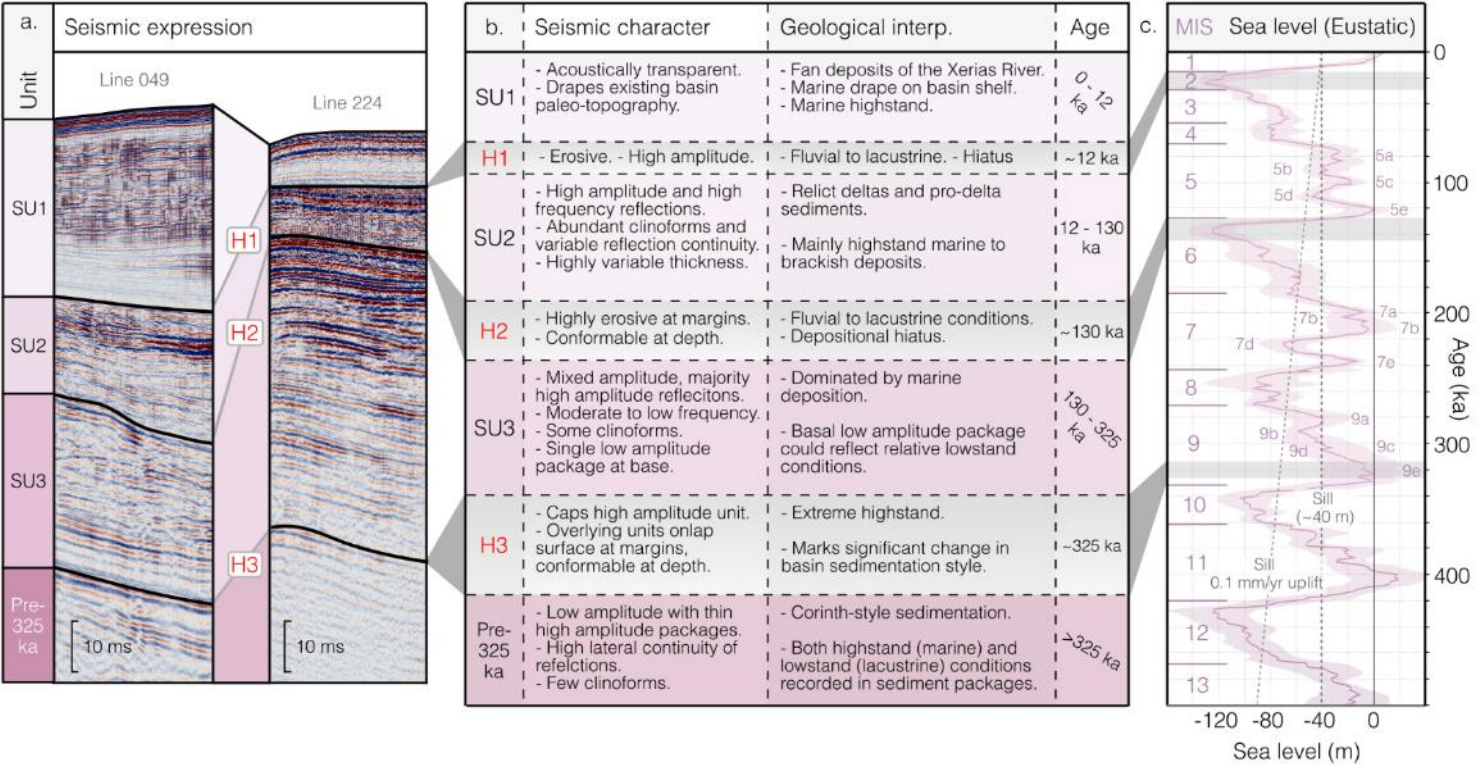
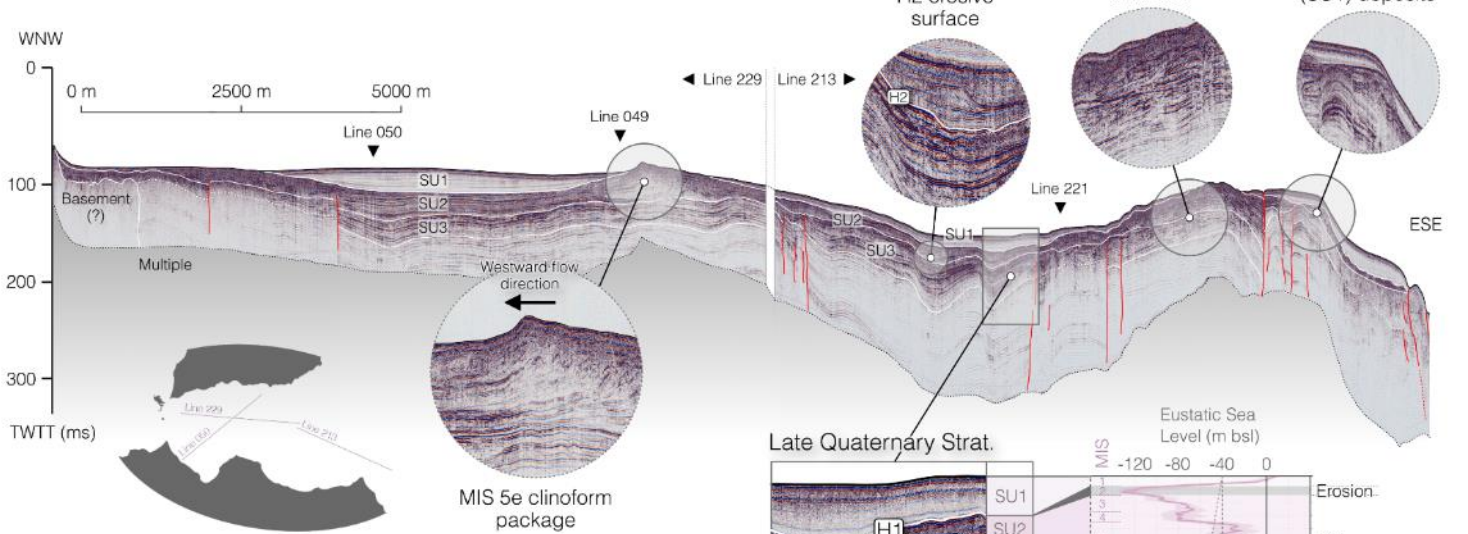
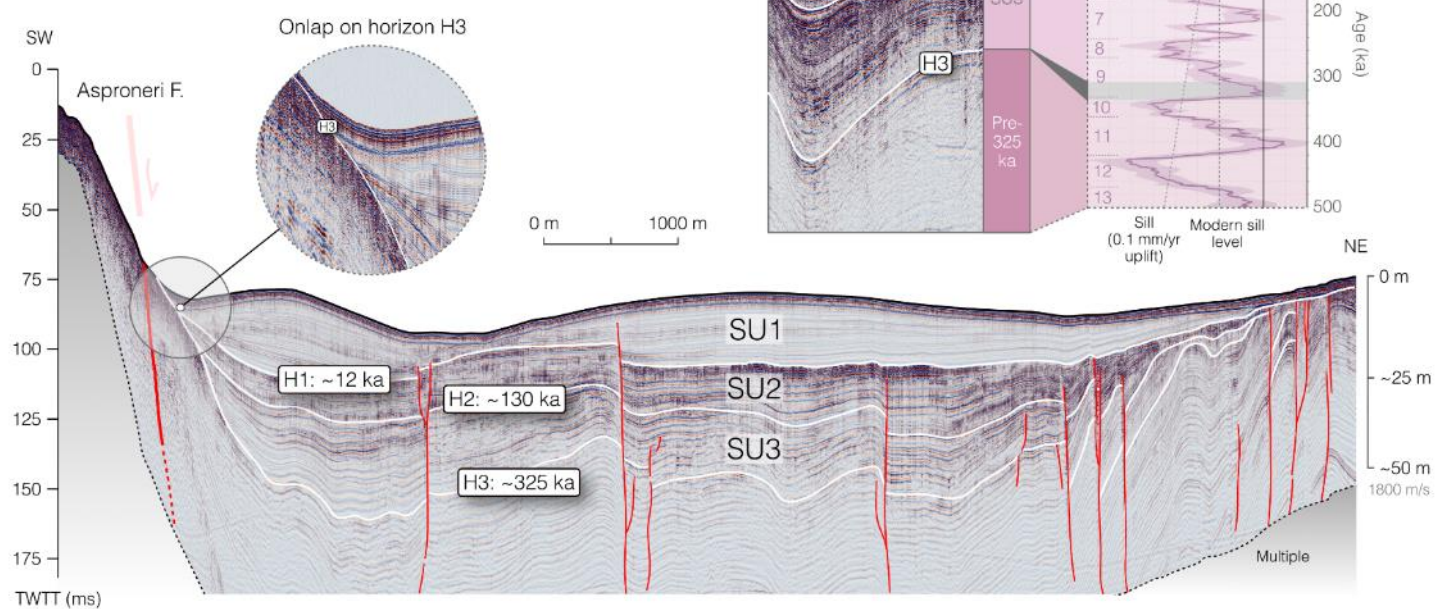


Figure 4: a. Seismic expression of upper syn-rift stratigraphy including seismic horizons (H1-3) and seismic units (SU1-3). b. Description of seismic character of each unit and horizon, geological interpretation of each unit and horizon and age attributed to each unit and horizon based on correlation to the eustatic sea level curve of Spratt and Lisiecki (2016) shown in c. Further seismic examples of mapped surfaces can be found in Supplementary Figure S2.

a. Axial seismic line: Line 213 & Line 229

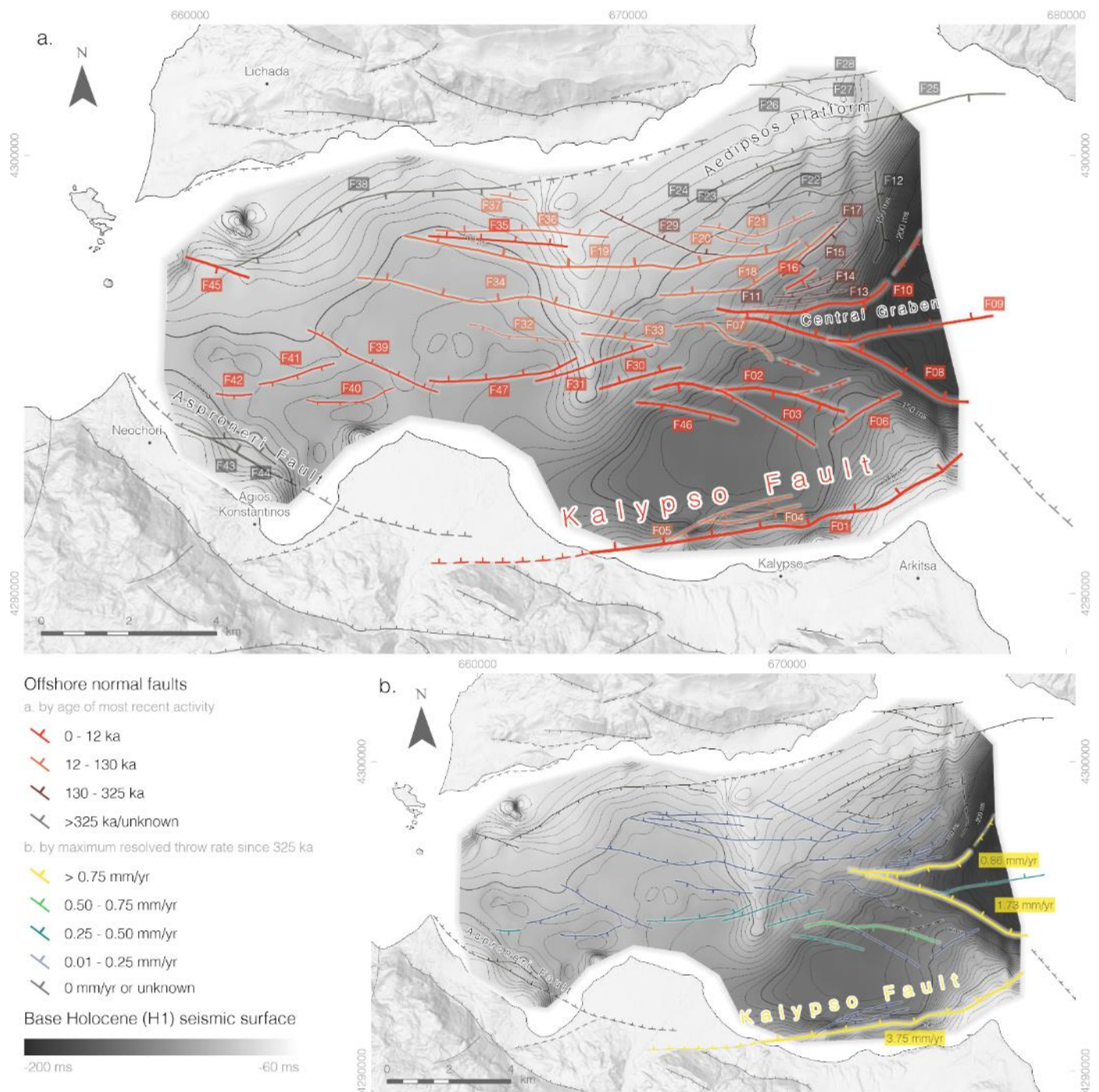


b. Across basin seismic line: Line 050



561

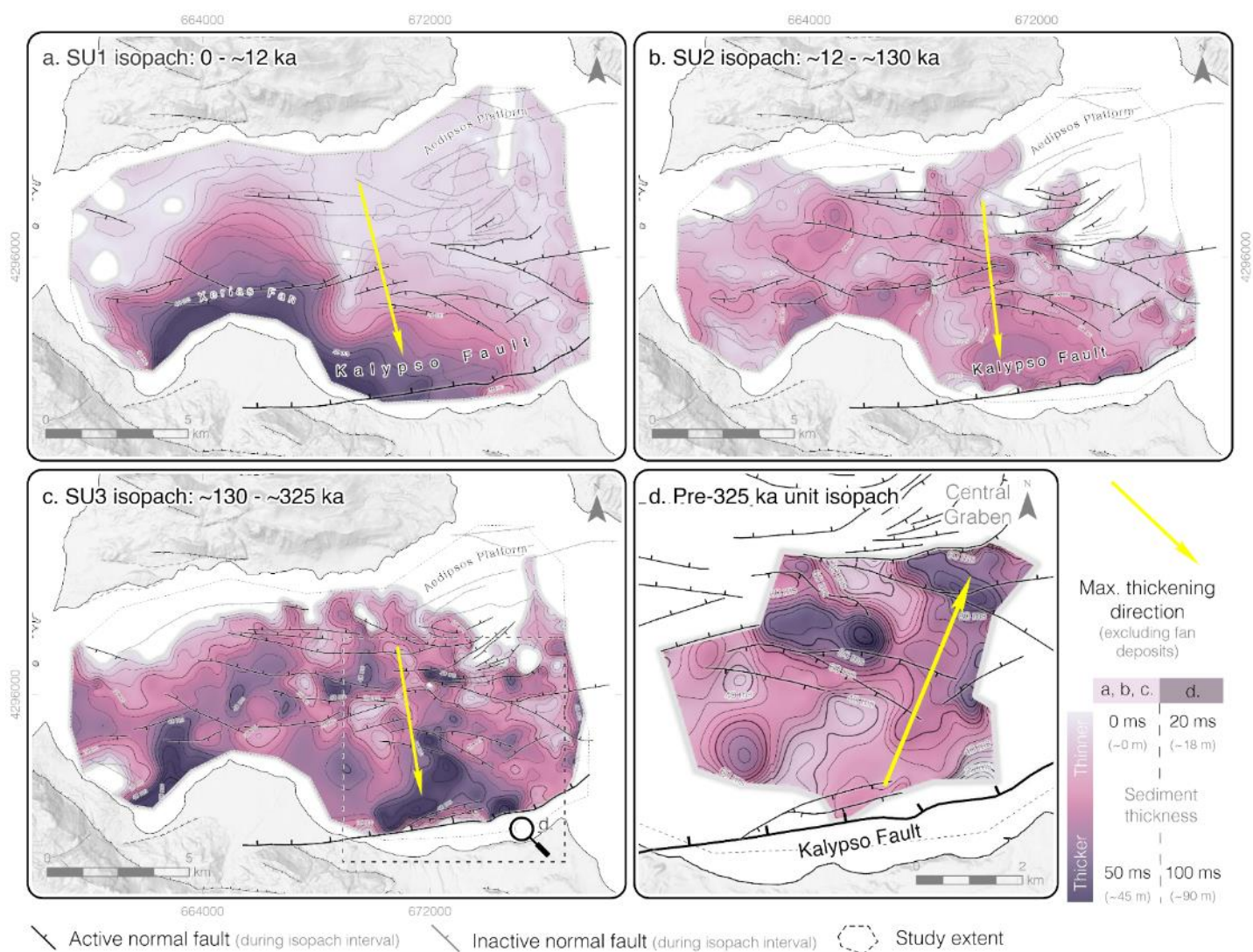
562 **Figure 5:** a) Axial seismic reflection profile along the Western Basin (Lines 213 and 229)
563 showing typical seismic sedimentary character, clinoform packages, variable Holocene
564 deposit styles, and major depocenter locations. Stratigraphic age correlation (Figure 3) shown
565 as inset with sea level from Spratt and Lisiecki (2016). b) Across-basin seismic reflection
566 profile (Line 050) showing basin structure including Asproneri Fault and high fault density in
567 NE. See Supplementary Figure S8 and S9 for uninterpreted seismic sections.



568

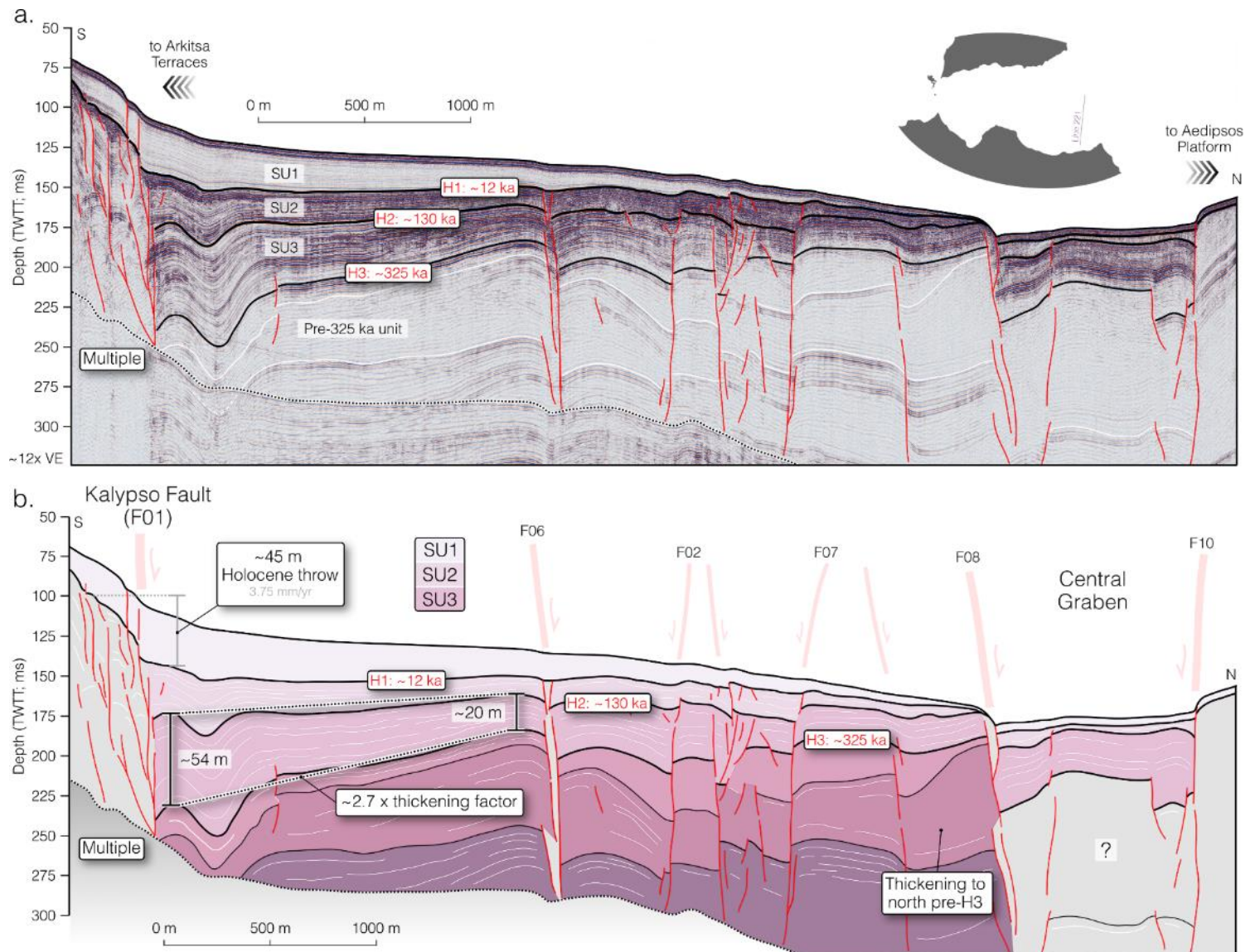
569 **Figure 6:** Map of offshore fault network identified in this study on depth to base Holocene
 570 (H1), effectively showing pre-Holocene basin geometry (without tectonic or compactional
 571 subsidence correction). a) Faults coloured by most recent activity based on offset of youngest
 572 key seismic horizon outlined in Figure 4. b) Faults coloured by maximum resolved throw rate
 573 over a given interval since ~325 ka (H3) based on throw rates calculated for each key seismic

574 horizon (H1-3). See Supplementary Figure S3 for detail on the generation the H1 surface and
 575 Supplementary Table S1 and S2 for further detail on each mapped structure.



576
 577 **Figure 7:** Isopach maps showing sediment thickness between the three major mapped
 578 surfaces in this study (a, b and c) and a package underlying the ~325 ka surface that is only
 579 apparent in the southeast of the study area (d). White area within study boundary indicates
 580 zero thickness.

581



582 **Figure 8:** a) Seismic reflection Line 221 with key surfaces (H1-3), seismic units (SU1-3) and
 583 faults shown. b) Interpreted section of line 221. The major Kalypso Fault Zone is shown in
 584 the south and active Central Graben in the north. SU1-3 thicken towards the Kalypso Fault
 585 (south), older packages with unassigned ages thicken towards the Central Graben (north). See
 586 Supplementary Figure S10 for uninterpreted seismic section.

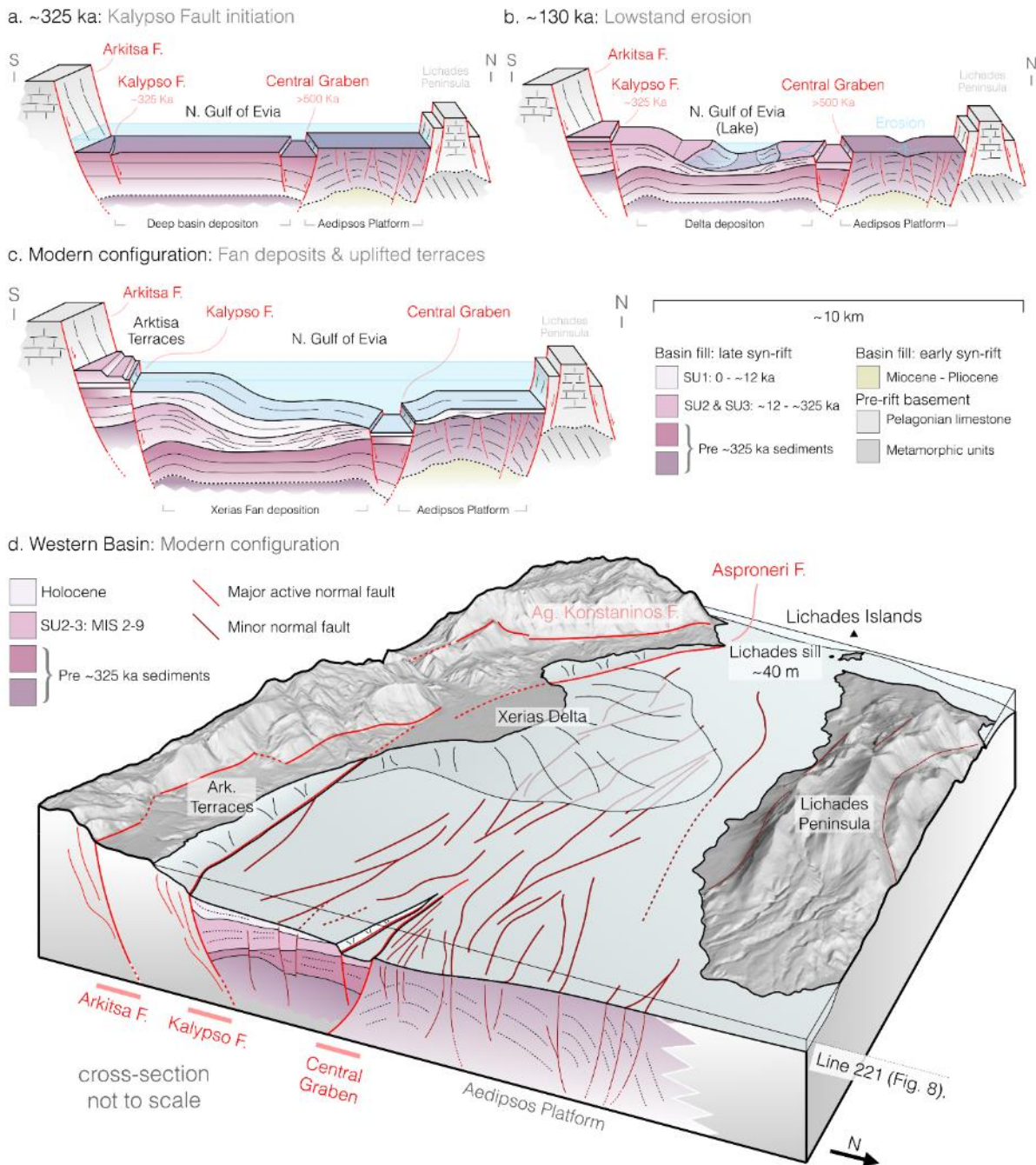


Figure 9: a-c) Schematic evolutionary block models showing structural and sedimentary development of the Western Basin near Arkitsa at ~325 ka (MIS 9e; b), ~130 ka (late-MIS 6; c) and the modern configuration of the basin (d). a) Three-dimensional summary model of the modern Western Basin of the North Gulf of Evia showing fault network, key structures and modern topography. 2x vertical exaggeration. Cross-section not to scale. Looking towards 240° at 25° pitch.

Acknowledgements

This work received funding as project DC12 of the TALENTS doctoral network through the European Union's HORIZON-MSCA-2022-DN-01 research and innovation program under grant agreement No. 101119486 (<https://www.talents-dn.eu>). JW, AW, RB, HK, and AG are beneficiaries of this grant. SC is funded by NERC grant NE/S007415/1 (Science and Solutions for a Changing Planet DTN). We are grateful to SLB for the provision of Petrel (Version 2024.4.0) for use in this project.

Data Availability

The fault network produced from this study is available as a .kml file. Uninterpreted seismic profiles presented in this study are available in the Supplementary Materials. Seismic reflection data is available on request.

References

- Armijo, R., Meyer, B., King, G.C.P., Rigo, A., Papanastassiou, D., 1996. Quaternary evolution of the Corinth Rift and its implications for the Late Cenozoic evolution of the Aegean. *Geophysical Journal International* 126, 11–53. <https://doi.org/10.1111/j.1365-246X.1996.tb05264.x>
- Bell, R.E., Duclaux, G., Nixon, C.W., Gawthorpe, R.L., McNeill, L.C., 2017. High-angle, not low-angle, normal faults dominate early rift extension in the Corinth Rift, central Greece. *Geology* 46, 115–118. <https://doi.org/10.1130/G39560.1>
- Bell, R.E., McNeill, L.C., Bull, J.M., Henstock, T.J., 2008. Evolution of the offshore western Gulf of Corinth. *GSA Bulletin* 120, 156–178. <https://doi.org/10.1130/B26212.1>
- Bell, R.E., McNeill, L.C., Bull, J.M., Henstock, T.J., Collier, R.E.L., Leeder, M.R., 2009. Fault architecture, basin structure and evolution of the Gulf of Corinth Rift, central Greece. *Basin Research* 21, 824–855. <https://doi.org/10.1111/j.1365-2117.2009.00401.x>
- Bradley, K.E., Vassilakis, E., Hosa, A., Weiss, B.P., 2013. Segmentation of the Hellenides recorded by Pliocene initiation of clockwise block rotation in Central Greece. *Earth and Planetary Science Letters* 362, 6–19. <https://doi.org/10.1016/j.epsl.2012.11.043>
- Briole, P., Ganas, A., Elias, P., Dimitrov, D., 2021. The GPS velocity field of the Aegean. New observations, contribution of the earthquakes, crustal blocks model. *Geophysical Journal International* 226, 468–492. <https://doi.org/10.1093/gji/ggab089>

- Brune, S., Kolawole, F., Olive, J.-A., Stamps, D.S., Buck, W.R., Buiter, S.J.H., Furman, T., Shillington, D.J., 2023. Geodynamics of continental rift initiation and evolution. *Nature Reviews Earth & Environment* 4, 235–253. <https://doi.org/10.1038/s43017-023-00391-3>
- Caroir, F., Chanier, F., Gaullier, V., Sakellariou, D., Bailleul, J., Maillard, A., Paquet, F., Watremez, L., Averbuch, O., Graveleau, F., Ferrière, J., 2024. Late Quaternary deformation in the western extension of the North Anatolian Fault (North Evia, Greece): Insights from very high-resolution seismic data (WATER surveys). *Tectonophysics* 870, 230138–230138. <https://doi.org/10.1016/j.tecto.2023.230138>
- Catuneanu, O., 2002. Sequence stratigraphy of clastic systems: concepts, merits, and pitfalls. *Journal of African Earth Sciences* 35, 1–43. [https://doi.org/10.1016/S0899-5362\(02\)00004-0](https://doi.org/10.1016/S0899-5362(02)00004-0)
- [dataset] Chanier, F., Gaullier, V., 2017. WATER cruise, Téthys II R/V, Sismar. <https://doi.org/10.17600/17009400>
- [dataset] Chanier, F., Watremez, L., 2021. WATER 2 cruise, RV Téthys II. <https://doi.org/doi.org/10.17600/18001115>
- Chousianitis, K., Sboras, S., Mouslopoulou, V., Chouliaras, G., Hristopulos, D.T., 2024. The Upper Crustal Deformation Field of Greece Inferred From GPS Data and Its Correlation With Earthquake Occurrence. *Journal of Geophysical Research: Solid Earth* 129, e2023JB028004. <https://doi.org/10.1029/2023JB028004>
- Coveney, S.M., Bell, R.E., Wils, K., Lastras, G., Whittaker, A.C., 2025. The Early Evolution of a Young Normal Fault in the Aysén Fjord, Chile. *Tectonics* 44, e2025TC008835. <https://doi.org/10.1029/2025TC008835>
- Cundy, A.B., Gaki-Papanastassiou, K., Papanastassiou, D., Maroukian, H., Frogley, M.R., Cane, T., 2010. Geological and geomorphological evidence of recent coastal uplift along a major Hellenic normal fault system (the Kamena Vourla fault zone, NW Evoikos Gulf, Greece). *Marine Geology* 271, 156–164. <https://doi.org/10.1016/j.margeo.2010.02.009>
- de Gelder, G., Fernández-Blanco, D., Melnick, D., Duclaux, G., Bell, R.E., Jara-Muñoz, J., Armijo, R., Lacassin, R., 2019. Lithospheric flexure and rheology determined by climate cycle markers in the Corinth Rift. *Sci Rep* 9, 4260. <https://doi.org/10.1038/s41598-018-36377-1>
- Drinia, H., Antonarakou, A., Anastasakis, G., 2014. Late Quaternary micropalaeontological record of a semi-enclosed marine basin, North Evoikos, central Aegean Sea. *Quaternary International* 345, 18–31. <https://doi.org/10.1016/j.quaint.2014.04.011>
- Feng, Y., Jiang, S., Hu, S., Li, S., Lin, C., Xie, X., 2016. Sequence stratigraphy and importance of syndepositional structural slope-break for architecture of Paleogene syn-rift lacustrine strata, Bohai Bay Basin, E. China. *Marine and Petroleum Geology* 69, 183–204. <https://doi.org/10.1016/j.marpetgeo.2015.10.013>
- Fernández-Blanco, D., de Gelder, G., Lacassin, R., Armijo, R., 2019. A new crustal fault formed the modern Corinth Rift. *Earth-Science Reviews* 199, 102919. <https://doi.org/10.1016/j.earscirev.2019.102919>
- Freitag, K., Reicherter, K., 2019. The earthquake and tsunami of 426 BC in Greece: observations by Thucydides and contextual interpretations. *Zeitschrift für Geomorphologie, Supplementary Issues* 62, 47–62. https://doi.org/10.1127/zfg_suppl/2019/0625
- Galanakis, D., Sboras, S., Sakellariou, D., Pavlides, S., Iordanidou, K., Georgiou, C., Ganas, A., Koukouvelas, I., Kranis, C., Lalechos, S., Rondoyanni, T., Lekkas, E., 2025. The Hellenic DataBase of Active Faults (HeDBAF): a new, national geodatabase of active

- faults for the broader Greek territory. Presented at the EGU 2025, Copernicus Meetings, Vienna. <https://doi.org/10.5194/egusphere-egu25-9230>
- Ganas, A., Karastathis, V., Moshou, A., Valkaniotis, S., Mouzakiotis, E., Papathanassiou, G., 2014. Aftershock relocation and frequency–size distribution, stress inversion and seismotectonic setting of the 7 August 2013 M=5.4 earthquake in Kallidromon Mountain, central Greece. *Tectonophysics* 617, 101–113. <https://doi.org/10.1016/j.tecto.2014.01.022>
- Ganas, A., Mouzakiotis, E., Moshou, A., Karastathis, V., 2016. Left-lateral shear inside the North Gulf of Evia Rift, Central Greece, evidenced by relocated earthquake sequences and moment tensor inversion. *Tectonophysics* 682, 237–248. <https://doi.org/10.1016/j.tecto.2016.05.031>
- Ganas, A., Oikonomou, I.A., Tsimi, C., 2013. NOAfaults: a digital database for active faults in Greece. *Bulletin of the Geological Society of Greece* 47, 518–530. <https://doi.org/10.12681/bgsg.11079>
- Ganas, A., Roberts, G.P., Memou, T., 1998. Segment boundaries, the 1894 ruptures and strain patterns along the Atalanti Fault, Central Greece. *Journal of Geodynamics* 26, 461–486. [https://doi.org/10.1016/S0264-3707\(97\)00066-5](https://doi.org/10.1016/S0264-3707(97)00066-5)
- Gawthorpe, R.L., Andrews, J.E., Collier, R.E.L., Ford, M., Henstra, G.A., Kranis, H., Leeder, M.R., Muravchik, M., Skourtsos, E., 2017. Building up or out? Disparate sequence architectures along an active rift margin—Corinth rift, Greece. *Geology* 45, 1111–1114. <https://doi.org/10.1130/G39660.1>
- Gawthorpe, R.L., Leeder, M.R., 2000. Tectono-sedimentary evolution of active extensional basins. *Basin Research* 12, 195–218. <https://doi.org/10.1111/j.1365-2117.2000.00121.x>
- Gawthorpe, R.L., Leeder, M.R., Kranis, H., Skourtsos, E., Andrews, J.E., Henstra, G.A., Mack, G.H., Muravchik, M., Turner, J.A., Stamatakis, M., 2018. Tectono-sedimentary evolution of the Plio-Pleistocene Corinth rift, Greece. *Basin Research* 30, 448–479. <https://doi.org/10.1111/bre.12260>
- Goldsworthy, M., Jackson, J., Haines, J., 2002. The continuity of active fault systems in Greece. *Geophysical Journal International* 148, 596–618. <https://doi.org/10.1046/j.1365-246X.2002.01609.x>
- Hatzfeld, D., Ziazia, M., Kementzetzidou, D., Hatzidimitriou, P., Panagiotopoulos, D., Makropoulos, K., Papadimitriou, P., Deschamps, A., 1999. Microseismicity and focal mechanisms at the western termination of the North Anatolian Fault and their implications for continental tectonics. *Geophysical Journal International* 137, 891–908. <https://doi.org/10.1046/j.1365-246x.1999.00851.x>
- IGME, 2006. Geological Map of Greece, 1:50,000 Scale (Pelasia sheet, 2006; Istaia sheet, 1984; Elatia sheet, 1967; Atalanti sheet, 1965).
- Jackson, Christopher A.-L., Bell, R.E., Rotevatn, A., Tvedt, A.B.M., 2017. Techniques to determine the kinematics of synsedimentary normal faults and implications for fault growth models, in: Childs, C., Holdsworth, R.E., Jackson, C. A.-L., Manzocchi, T., Walsh, J.J., Yielding, G. (Eds.), *The Geometry and Growth of Normal Faults*. The Geological Society of London, p. 0. <https://doi.org/10.1144/SP439.22>
- Jolivet, L., Faccenna, C., Huet, B., Labrousse, L., Le Pourhiet, L., Lacombe, O., Lecomte, E., Burov, E., Denèle, Y., Brun, J.-P., Philippon, M., Paul, A., Salaün, G., Karabulut, H., Piromallo, C., Monié, P., Gueydan, F., Okay, A.I., Oberhänsli, R., Pourteau, A., Augier, R., Gadenne, L., Driussi, O., 2013. Aegean tectonics: Strain localisation, slab tearing and trench retreat. *Tectonophysics, The Aegean: a natural laboratory for tectonics - Neotectonics* 597–598, 1–33. <https://doi.org/10.1016/j.tecto.2012.06.011>

- Kranis, H., 2007. Neotectonic Basin Evolution in Central-Eastern Mainland Greece: An Overview. *Bulletin of the Geological Society of Greece* 40, 360–373.
<https://doi.org/10.12681/bgsg.16621>
- Kranis, H., Palyvos, N., Livaditis, G., Maroukian, H., 2001. The Hyambolis zone: geomorphological and tectonic evidence of a transverse structure in Lokris (Central Greece). *Bulletin of the Geological Society of Greece* 34, 251–251.
<https://doi.org/10.12681/bgsg.17020>
- Lykousis, V., Sakellariou, D., Moretti, I., Kaberi, H., 2007a. Late Quaternary basin evolution of the Gulf of Corinth: Sequence stratigraphy, sedimentation, fault–slip and subsidence rates. *Tectonophysics, Deep structure, fault arrays and surface processes within an active graben: The Gulf of Corinth* 440, 29–51.
<https://doi.org/10.1016/j.tecto.2006.11.007>
- Lykousis, V., Sakellariou, D., Moretti, I., Kaberi, H., 2007b. Late Quaternary basin evolution of the Gulf of Corinth: Sequence stratigraphy, sedimentation, fault–slip and subsidence rates. *Tectonophysics* 440, 29–51.
<https://doi.org/10.1016/j.tecto.2006.11.007>
- McNeill, L.C., Collier, R.E.LI., De Martini, P.M., Pantosti, D., D’Addezio, G., 2005. Recent history of the Eastern Eliki Fault, Gulf of Corinth: geomorphology, palaeoseismology and impact on palaeoenvironments. *Geophysical Journal International* 161, 154–166.
<https://doi.org/10.1111/j.1365-246X.2005.02559.x>
- McNeill, L.C., Shillington, D.J., Carter, G.D.O., Everest, J.D., Gawthorpe, R.L., Miller, C., Phillips, M.P., Collier, R.E.LI., Cvetkoska, A., De Gelder, G., Diz, P., Doan, M.-L., Ford, M., Geraga, M., Gillespie, J., Hemelsdaël, R., Herrero-Bervera, E., Ismaiel, M., Janikian, L., Kouli, K., Le Ber, E., Li, S., Maffione, M., Mahoney, C., Machlus, M.L., Michas, G., Nixon, C.W., Oflaz, S.A., Omale, A.P., Panagiotopoulos, K., Pechlivanidou, S., Sauer, S., Seguin, J., Sergiou, S., Zakharova, N.V., Green, S., 2019. High-resolution record reveals climate-driven environmental and sedimentary changes in an active rift. *Scientific Reports* 9, 3116–3116.
<https://doi.org/10.1038/s41598-019-40022-w>
- Mildon, Z.K., Diercks, M., Roberts, G.P., Faure Walker, J.P., Ganas, A., Papanikolaou, I., Sakas, V., Robertson, J., Sgambato, C., Mitchell, S., 2024. Transient Aseismic Vertical Deformation Across the Steeply-Dipping Pisias-Skinos Normal Fault (Gulf of Corinth, Greece). *Tectonics* 43, e2024TC008276–e2024TC008276.
<https://doi.org/10.1029/2024TC008276>
- Nixon, C.W., McNeill, L.C., Bull, J.M., Bell, R.E., Gawthorpe, R.L., Henstock, T.J., Christodoulou, D., Ford, M., Taylor, B., Sakellariou, D., Ferentinos, G., Papatheodorou, G., Leeder, M.R., Collier, R.E.L.I., Goodliffe, A.M., Sachpazi, M., Kranis, H., 2016. Rapid spatiotemporal variations in rift structure during development of the Corinth Rift, central Greece. *Tectonics* 35, 1225–1248.
<https://doi.org/10.1002/2015TC004026>
- Nixon, C.W., McNeill, L.C., Gawthorpe, R.L., Shillington, D.J., Michas, G., Bell, R.E., Moyle, A., Ford, M., Zakharova, N.V., Bull, J.M., de Gelder, G., 2024. Increasing fault slip rates within the Corinth Rift, Greece: A rapidly localising active rift fault network. *Earth and Planetary Science Letters* 636, 118716.
<https://doi.org/10.1016/j.epsl.2024.118716>
- Palyvos, N., Bantekas, I., Kranis, H., 2006. Transverse fault zones of subtle geomorphic signature in northern Evia island (central Greece extensional province): An introduction to the Quaternary Nileas graben. *Geomorphology* 76, 363–374.
<https://doi.org/10.1016/j.geomorph.2005.12.002>

- Pantosti, D., De Martini, P.M., Papanastassiou, D., Lemeille, F., Palyvos, N., Stavrakakis, G., 2004. Paleoseismological Trenching across the Atalanti Fault (Central Greece): Evidence for the Ancestors of the 1894 Earthquake during the Middle Ages and Roman Times. *Bulletin of the Seismological Society of America* 94, 531–549. <https://doi.org/10.1785/0120020207>
- Papanastassiou, D., Cundy, A.B., Gaki-Papanastassiou, K., Frogley, M.R., Tsanakas, K., Maroukian, H., 2014. The Uplifted Terraces of the Arkitsa Region, NW Evoikos Gulf, Greece: A Result of Combined Tectonic and Volcanic Processes? *The Journal of Geology* 122, 397–410. <https://doi.org/10.1086/676595>
- Papanikolaou, D., 2021. The Geology of Greece. <https://doi.org/10.1007/978-3-030-60731-9>
- Pechlivanidou, S., Cowie, P.A., Hannisdal, B., Whittaker, A.C., Gawthorpe, R.L., Pennos, C., Rüser, O.S., 2018. Source-to-sink analysis in an active extensional setting: Holocene erosion and deposition in the Sperchios rift, central Greece. *Basin Research* 30, 522–543. <https://doi.org/10.1111/bre.12263>
- Pirazzoli, P.A., Stiros, S.C., Arnold, M., Laborel, J., Laborel-Deguen, F., 1999. Late holocene coseismic vertical displacements and tsunami deposits near Kynos, Gulf of Euboea, Central Greece. *Physics and Chemistry of the Earth, Part A: Solid Earth and Geodesy* 24, 361–367. [https://doi.org/10.1016/S1464-1895\(99\)00042-3](https://doi.org/10.1016/S1464-1895(99)00042-3)
- Roberts, G.P., Ganas, A., 2000. Fault-slip directions in central and southern Greece measured from striated and corrugated fault planes: Comparison with focal mechanism and geodetic data. *Journal of Geophysical Research: Solid Earth* 105, 23443–23462. <https://doi.org/10.1029/1999JB900440>
- Roberts, S., Jackson, J., 1991. Active normal faulting in central Greece: an overview. *Geological Society, London, Special Publications* 56, 125–142. <https://doi.org/10.1144/GSL.SP.1991.056.01.09>
- Sakellariou, D., Rousakis, G., Kaberi, H., Kapsimalis, V., Georgiou, P., Kanellopoulos, Th., Lykousis, V., 2007. Tectono-Sedimentary Structure and Late Quaternary Evolution Of The North Evia Gulf Basin, Central Greece: Preliminary Results. *Bulletin of the Geological Society of Greece* 40, 451–462. <https://doi.org/10.12681/bgsg.16644>
- Sboras, S., Mouzakiotis, E., Chousianitis, K., Karastathis, V., Evangelidis, C.P., Lazos, I., Papageorgiou, A., Liakopoulos, S., Iordanidou, K., 2025. Where does the active North Aegean Sea shear stop? Geodynamic and seismotectonic implications from recent strike-slip earthquake occurrences and GPS-based geodetic analysis in Euboea, Phthiotis and Boeotia, Central Greece. *Tectonophysics* 914, 230917. <https://doi.org/10.1016/j.tecto.2025.230917>
- Spratt, R.M., Lisiecki, L.E., 2016. A Late Pleistocene sea level stack. *Climate of the Past* 12, 1079–1092. <https://doi.org/10.5194/cp-12-1079-2016>
- Vail, P.R., Mitchum, R.M., Jr., Thompson, S., III, 1977. Seismic Stratigraphy and Global Changes of Sea Level, Part 4: Global Cycles of Relative Changes of Sea Level, in: Payton, C.E. (Ed.), *Seismic Stratigraphy — Applications to Hydrocarbon Exploration*. American Association of Petroleum Geologists, p. 0. <https://doi.org/10.1306/M26490C6>
- Van Andel, T. H., Perissoratis, C., 2006. Late Quaternary depositional history of the North Evvoikos Gulf, Aegean Sea, Greece. *Marine Geology* 232, 157–172. <https://doi.org/10.1016/j.margeo.2006.07.004>
- Walker, R.T., Claisse, S., Telfer, M., Nissen, E., England, P., Bryant, C., Bailey, R., 2010. Preliminary estimate of Holocene slip rate on active normal faults bounding the southern coast of the Gulf of Evia, central Greece. *Geosphere* 6, 583–593. <https://doi.org/10.1130/GES00542.1>

- Watkins, S.E., Whittaker, A.C., Bell, R.E., McNeill, L.C., Gawthorpe, R.L., Brooke, S.A.S., Nixon, C.W., 2018. Are landscapes buffered to high-frequency climate change? A comparison of sediment fluxes and depositional volumes in the Corinth Rift, central Greece, over the past 130 k.y. *GSA Bulletin* 131, 372–388. <https://doi.org/10.1130/B31953.1>
- Wells, D.L., Coppersmith, K.J., 1994. New empirical relationships among magnitude, rupture length, rupture width, rupture area, and surface displacement. *Bulletin of the Seismological Society of America* 84, 974–1002. <https://doi.org/10.1785/BSSA0840040974>
- Whittaker, A.C., Walker, A.S., 2015. Geomorphic constraints on fault throw rates and linkage times: Examples from the Northern Gulf of Evia, Greece. *Journal of Geophysical Research: Earth Surface* 120, 137–158. <https://doi.org/10.1002/2014JF003318>
- Wood, J., Whittaker, A.C., Bell, R.E., Coveney, S.M., Kranis, H.D., 2025. Resolving Coseismic and Aseismic Normal Fault Slip Behaviors From InSAR Time Series of the European Ground Motion Service (EGMS). *Tectonics* 44, e2025TC008904. <https://doi.org/10.1029/2025TC008904>
- Xu, G., Haq, B.U., 2022. Seismic facies analysis: Past, present and future. *Earth-Science Reviews* 224, 103876. <https://doi.org/10.1016/j.earscirev.2021.103876>